UC Berkeley
UC Berkeley Previously Published Works

Title

Challenges for density functional theory: calculation of CO adsorption on electrocatalytically relevant metals

Permalink

Journal

ISSN

Authors

Lininger, Christianna N
Gauthier, Joseph A
Li, Wan-Lu
et al.

Publication Date

DOI

Challenges for density functional theory: calculation of CO adsorption on electrocatalytically relevant metals†

Christianna N. Lininger, [ab] Joseph A. Gauthier, [ab] Wan-Lu Li, [ac]
Elliot Rossomme, [c] Valerie Vaissier Welborn, [cd] Zhou Lin, [ac]
Teresa Head-Gordon, *[abce] Martin Head-Gordon *[ac] and
Alexis T. Bell *[ab]

Density Functional Theory (DFT) is currently the most tractable choice of theoretical model used to understand the mechanistic pathways for electrocatalytic processes such as CO_2 or CO reduction. Here, we assess the performance of two DFT functionals designed specifically to describe surface interactions, RTPSS and RPBE, as well as two popular meta-GGA functionals, SCAN and B97M-rV, that have not been *a priori* optimized for better interfacial properties. We assess all four functionals against available experimental data for prediction of bulk and bare surface properties on four electrocatalytically relevant metals, Au, Ag, Cu, and Pt, and for binding CO to surfaces of these metals. To partially mitigate issues such as thermal and anharmonic corrections associated with comparing computations with experiments, molecular benchmarks against high level quantum chemistry are reported for CO complexes with Au, Ag, Cu and Pt atoms, as well as the CO–water complex and the water dimer. Overall, we find that the surface modified RPBE functional performs reliably for many of the benchmarks examined here, and the meta-GGA functionals also show promising results. Specifically B97M-rV predicts the correct site preference for CO binding on Ag and Au (the only functional tested here to do so), while RTPSS performs well for surface relaxations and binding of CO on Pt and Cu.

1 Introduction

The electrochemical reduction of CO_2 offers a powerful means for converting this greenhouse gas into useful chemicals and fuels through a closed carbon cycle that utilizes renewable energy (wind and solar) to drive the reaction. Experimental studies of the electrochemical CO_2 reduction reaction (CO2RR) have been devoted to identifying the catalyst compositions that exhibit high activity and selectivity for forming desired products, such as CO/H_2, HCOOH, CH_4, C_2H_4, and C_2H_5OH.[1–5] However, it has

proven more difficult for experiments to probe the detailed mechanisms and kinetics by which CO_2 reacts to form the observed products due to the (very) low concentrations of adsorbed intermediates and the lack of adequately surface-sensitive spectroscopic techniques. By contrast, the application

[a] *Chemical Sciences Division, Lawrence Berkeley National Laboratory, Berkeley, California 94720, USA. E-mail: alexbell@berkeley.edu, mhg@cchem.berkeley.edu, thg@berkeley.edu; Tel: +1-(510)-642-1536*

[b] *Department of Chemical and Biomolecular Engineering, University of California, Berkeley, California 94720, USA*

[c] *Kenneth S. Pitzer Center for Theoretical Chemistry, Department of Chemistry, University of California, Berkeley, California 94720, USA*

[d] *Department of Chemistry, Virginia Tech, Blacksburg, VA 26067, USA*

[e] *Department of Bioengineering, University of California, Berkeley, California 94720, USA*
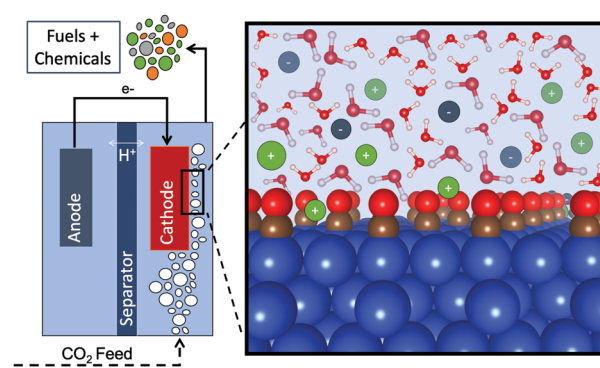
Fig. 1 (left) Fuel cell for CO_2 reduction. (right) Cartoon for the electrode-electrolyte interface with CO molecules at the atop position of a (111) metal surface.

of theoretical methods have proven far more effective in providing mechanistic insights.

Fig. 1 shows an electrochemical cell used to conduct the CO2RR in an aqueous electrolyte. CO_2 is fed into the cathode compartment and products are removed in the effluent. The right-hand side of the figure depicts a cartoon of the electrode–electrolyte interface. A complete theoretical description of the CO2RR requires a multiscale, multiphysics model that includes the rates of elementary processes occurring on the catalyst surface, a representation of the electrostatic field created by charge imbalance in the Helmholtz double layer, and (at high current densities) a description of the rates of ionic and neutral species transport through the mass-transfer boundary layer at the electrode–electrolyte interface. However, it is very difficult to test the accuracy of the whole model because the number of experimental observables is limited, the primary observable being the macroscopic measurements of product current density *versus* applied voltage. Therefore, each level of theory making up the components of a multiscale model needs to be validated for its intrinsic accuracy.

To illustrate the difficulties, we note that multiphysics models require the evaluation of the free energy of activation to determine the rate coefficients for elementary reaction, which are then incorporated into a micro-kinetic model of the reactions leading from reactants to final products.[6–9] These free energies are typically obtained from Density Functional Theory (DFT) calculations[10] at the level of the semi-local generalized gradient approximation (GGA). It has become more standard for DFT simulations to also include the implicit effects of liquid solvent through (modified) versions of the Poisson Boltzmann equation (PBE),[7,11–14] or employing explicit molecular solvent as part of the PBE description.[15–17] A number of recent DFT studies, have also enabled prediction of the reaction energetics as a function of applied bias.[14,17–24]

Previous theoretical investigations have revealed some of the shortcomings of the GGA functionals for molecular and surface chemistry.[25–37] Such effects originate from the inexact form of the exchange–correlation functional, which leads to the well-known fractional charge and fractional spin errors.[38–40] For surface-adsorbate systems, predicted properties with GGAs have known problems in accurate prediction of barrier heights,[29] surface energies,[31] and band gaps.[32,39] Issues relevant to the modeling of CO_2 reduction in particular are poorly described adsorption energies[33–35] and the inability to correctly predict adsorption-site preference.[31,34,36,37]

The aim of the present study is to investigate the accuracy of newer DFT functionals for determining the structural and physical properties of metals commonly used for the CO2RR and their interactions with a catalytically relevant adsorbate, CO. More specifically, we examine two DFT functionals that have been explicitly modified for better reproduction of surface interactions, the GGA RPBE[33] and the meta-GGA RTPSS.[41] We also examine two new meta-GGA functionals, B97M-rV[42,43] which performs well for weak interactions and molecular systems,[10] and SCAN,[44] which performs well for condensed matter problems. Neither B97M-rV nor SCAN is modified explicitly for surface

interactions. We have characterized these DFT functionals over a range of metals with different surface properties, Au, Ag, Cu, and Pt, in order to capture strong binding (Pt), intermediate binding (Cu), and relatively weak binders (Au and Ag) to CO. B97M-rV includes the rVV10 non-local correlation, which has been shown to more accurately reproduce weakly bound systems.[43,45]

We have chosen to benchmark the properties of CO since it is observed along CO_2 reduction pathways as an end product on Ag, Au, and Zn[5,46–48] or as an intermediate in the formation of C_{1+} products on Cu.[5,47,48] We also note that there are many experimental studies of the heats of adsorption, vibrational frequency, and structural changes to both CO and the metal surfaces upon CO adsorption. For these reasons, CO adsorption on metals has served as a benchmark for many surface-science theoretical studies.[49] We also note that errors in predicting the strength of CO adsorption, the site preference for CO adsorption (atop *vs.* bridging *vs.* hollow sites), and the resulting vibrational frequencies, can have significant influence on the calculated free energies relevant to the multi-physics model and, hence, on the kinetics of CO hydrogenation to hydrocarbons and oxygenated products.

The results of our investigations serve to identify the shortcomings as well as the strengths of DFT calculations targeted for input into multiscale/multiphysics models of the CO2RR. We assess the errors attributable to the choice of functional and/or theoretical framework used to describe bulk metal parameters, surface relaxations, and adsorbate binding properties. These results also provide a general framework for developing a more complete solid–liquid interface model not only for the CO2RR but also for other electrochemical processes, such as the oxygen reduction reaction.

2 Methods

2.1 DFT methodology and functionals

We have used the Vienna Ab-Initio Simulation Package (VASP)[50,51] to perform the Kohn–Sham DFT calculations. The VASP[50,51] projector augmented wave (PAW)[51] methods are as follows. The exchange–correlation potential was described with four different functional forms, RPBE,[33] RTPSS,[41] SCAN,[44] and B97M-rV.[43] The plane-wave basis set cutoff and k-points scheme were determined for each functional independently, such that the energy converged to less than ∼3 meV per atom. The cutoffs utilized were 800 eV for RPBE, 750 eV for B97M-rV, and 850 eV for both RTPSS and SCAN. The Methfessel–Paxton smearing scheme of order 1 was used to sample the Brillouin zone with a γ-centered grid,[52] and a broadening parameter of 0.2 eV was used. The appropriate pseudopotentials for the levels of theory were utilized; specifically, as SCAN, RTPSS, and B97M-rV are all meta-GGA's, they require information on the kinetic energy density of the core electrons in the pseudopotentials, while RPBE as a GGA uses a pseudopotential that does not incorporate the kinetic energy density of the core electrons.

Benchmarking tests to determine the best practice for surface supercell construction were performed on the Ag(110) surface with the RPBE functional in VASP. The results of these benchmarking

tests were then applied to the other VASP calculations herein. The adsorption energy for CO on Ag(110) as a function of the total number of layers in the cell was calculated with four, six, or eight total layers. In addition, for each case (four, six, and eight), either two or three Ag surface layers were allowed to relax. Results indicated that the adsorption energy did not vary significantly as a function of two or three free layers at the surface (<0.1 kcal mol^{-1}). However, there was a ~ 1 kcal mol^{-1} difference in adsorption energy between a four-layer cell and a six-layer cell, and a ~ 0.2 kcal mol^{-1} difference between a six-layer and an eight-layer cell. Additionally, the adsorption energy was calculated as a function of surface coverage and found to vary by <0.1 kcal mol^{-1} between one CO adsorbed on a 2×2 surface and one CO adsorbed on a 3×3 Ag(110) surface. To optimize both accuracy and computational cost, the VASP surface supercells used herein consisted of five total layers of 2×2 metal atoms, with the top two layers allowed to relax, while the bottom three layers were frozen at the bulk structure. For comparison with low coverage experimental measurements[35,53-55] all adsorption calculations reported herein use a surface coverage of $\theta = 0.25$.

To validate some of the VASP results presented here, we performed computations on molecular metal monocarbonyls (MCOs, M = Ag, Au, Cu, Pt) using the Q-Chem package,[56] following previous work.[57] (ESI† in Section S1). DFT computations were completed with the RPBE,[33] SCAN,[44] B97M-rV,[43] and ωB97X-V[58] density functionals; coupled cluster with single, double, and perturbative triple excitations [CCSD(T)][59] were also performed. Unrestricted wave functions were used in all cases, and solutions were ensured to be stable with respect to mixing of the occupied and virtual orbital spaces. Self-consistent field (SCF) iterations were converged to a DIIS error of at most 10^{-10} Hartree, and CCSD(T) computations were taken to be converged when errors in the energy and magnitude of the T-amplitudes were at most 10^{-8} Hartree and 10^{-6}, respectively. For a given level of correlation, MCO complex geometries were optimized using the def2-TZVPD basis set,[60,61] and the absence of imaginary harmonic vibrational frequencies, determined through diagonalization of the full Hessian matrix, were used to confirm that each structure was a minimum. Single-point energy computations at these geometries were completed using the def2-TZVPPD[60,61] and def2-QZVPPD[60,62] basis sets. The def2-QZVPPD energies were taken to approximate the complete basis set (CBS) limit for Hartree–Fock and DFT energies, but a two-point CBS extrapolation scheme was used to determine the limiting behavior of the correlation energy, *viz.*

$$E_{\text{CBS}}(X) = E_X - AX^{-3}, \qquad (1)$$

where X is the cardinal number of the basis set, E_{CBS} is the CBS energy, and A is a constant that is determined through comparison of the def2-TZVPPD and def2-QZVPPD results. A representative metal carbonyl cluster is shown in Fig. 2c.

2.2 Surface supercell construction and benchmarking

Each bulk metal was fully relaxed for each DFT functional in VASP. Each metal surface was then created from the fully relaxed bulk metal lattice constant with the pymatgen package in Python.[63]
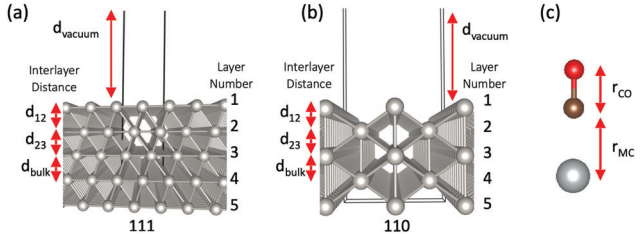

Fig. 2 Depiction of (a) (111) (b) (110) surfaces showing d_{12}, d_{23}, and d_{bulk} definitions and layer numbers and (c) the metal carbonyl complex motif showing r_{CO}, the distance between the carbon and oxygen and r_{MC}, the distance between the lone metal atom and the carbon atom.

We note that the equilibrium lattice constant for a given metal varies with exchange–correlation functional, and the surface supercell was therefore scaled according to the lattice constant for each respective functional. We relaxed the top two layers of only one of the surfaces in the supercell, while the rest of the atoms in the supercell were fixed at the equilibrium bulk structure. In Fig. 2, this corresponds to relaxing layers labeled 1 and 2 and freezing layers 3–5. In addition, the cell dimensions were fixed. A 30 Å vacuum was imposed above the surface to inhibit periodic image interaction. Additionally, the dipole correction flag in VASP was utilized to minimize interaction between periodic images. A representative surface supercell is shown in Fig. 2a.

2.3 Surface energies and potential of zero charge

The surface formation energy was calculated as:

$$\gamma = [E(M) - nE(M_{\text{bulk}})]/(2A), \qquad (2)$$

where $E(M)$ was the energy of the entire surface supercell relaxed according to the methods described in the previous section, $E(M_{\text{bulk}})$ was the energy of one metal atom in the bulk, n was the number of metal atoms in the entire surface supercell, and A was the area of each surface allowed to relax.[64] The potential of zero free charge (PZFC) was calculated for each metal surface as the difference between the work function for the metal solvated with VASPsol in an implicit 1 M electrolyte, following the protocol by Zhuang *et al.*[65] Note that when we refer to a DFT calculated PZC, we mean the PZFC without any species adsorption.

2.4 CO adsorption and vibrational frequencies

The energy for CO adsorption was calculated for the single metal atoms and on the (111) surfaces of Au, Ag, Cu, and Pt using VASP. For the surface adsorption, the CO molecule was placed at the atop, bridge, fcc-hollow, and hcp-hollow sites, carbon side down, and allowed to fully relax along with the top two layers of the metal surface, while the bottom metal layers were frozen at (functional dependent) bulk positions. The adsorption energy was calculated based on the reaction: M + CO$_{(g)} \rightarrow$ M–CO*, where M is the bare but relaxed metal surface, CO$_{(g)}$ is the fully relaxed CO molecule in vacuum, and M–CO* is the metal surface with adsorbed CO molecule where only CO and the top two layers of the metal have been allowed to relax. The adsorption

energy was calculated as $\Delta E_{ads} = E(M-CO^*) - E(CO_{(g)}) - E(M)$. Herein, adsorption energies are always reported per mole of CO and the surface coverage was always $\theta = 0.25$.

The adsorption energy was calculated analogously for the adsorption of CO to single metal atoms (Au, Ag, Cu, and Pt) based on the reaction: $M_{(g)} + CO_{(g)} \rightarrow M-CO_{(g)}$, where $M_{(g)}$ is the ground state for the single atom, $CO_{(g)}$ is the relaxed CO molecule, and $M-CO_{(g)}$ is the relaxed metal CO complex. The adsorption energy was calculated as $\Delta E_{ads} = E(M-CO_{(g)}) - E(CO_{(g)}) - E(M_{(g)})$.

All vibrational frequencies reported herein used the harmonic approximation. VASP was used to calculate all vibrational frequen-cies for all DFT functionals.

Fig. 4 Surface energy γ in eV Å^{-2} for each metal surface in Table 1.

3 Results and discussion

3.1 Bulk and surface metal properties

Bulk metal properties. We first compare the different DFT functionals to predict the bulk and surface properties of Au, Ag, Cu, and Pt. Lattice constants and percent differences from experimental values for the bulk metals were calculated and are reported in Fig. 3 and are tabulated in Section S2 of the ESI.† The error in the lattice constants calculated with RPBE (GGA) is worse than that for the three meta-GGA's, but all functionals yielded acceptable results.[66,67]

Metal surface properties: surface energy. The surface energy has been shown to be correlated with catalytic activity of transition metal and elemental metal catalysts for the hydrogen evolution reaction (HER). This correlation between surface energy and catalytic activity has been attributed to the surface energy serving as reporter for coordination saturation at the surface and therefore the surface reactivity.[65] Therefore, the ability of a DFT functional to reproduce experimentally observed surface energy trends has bearing on the ability of the functional to predict trends in adsorption energies.

Fig. 4 and Table 1 report surface energies for Ag(110) and Ag(111) as well as for the (111) surfaces of Au, Cu, and Pt. The experimental[68] surface energy differences between the (110) and (111) surfaces of Ag are small, with the (111) surface being 0.005 eV Å^{-2} more stable. Overall, RPBE and B97MrV had the minimum error with respect to the experimental values.

In a study examining the effect of surface strain on the reactivity of CO on Ru(001) surfaces,[69] a 0.15 eV increase in CO interaction
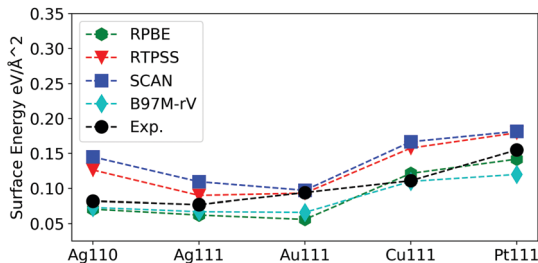
strength per 1% surface strain was found. This dependence of adsorbate interaction on the metal surface strain was attributed to the dependence of metal d states on the material strain. Since the metal d states are responsible for the bonding with the CO molecule, changes in those states will affect adsorption energetics and trends.[69] This effect can be leveraged experimentally to induce surface reactivity by controlling surface strain through deposition of metals with differing lattice constants. However, this effect can also lead to incorrect site-preference results in theoretical calculations that do not accurately simulate the metal surface.

Metal surface properties: surface relaxations. Fig. 5 and Table 1 present the calculated layer–layer relaxations as percent changes relative to the functional dependent layer–layer distances in the bulk. The distance between the first and second layers and the second and third layers, d_{12} and d_{23}, respectively, as well as the total relaxation of the first two surface layers, d_{13}, were compared to experiment. For the Ag(111) surface, the experimental measurements are either reported as d_{12} at -2.5% and d_{23} at -0.6%,[70] shown with black data points in Fig. 5, or the relaxations are reported as d_{12} at $<-2\%$,[71] shown with a black line in Fig. 5.

B97M-rV consistently overestimates the relaxation for all surfaces. As shown in Fig. 5, with the exception of B97M-rV, all functionals tested predicted very little relaxation of the d_{12} and d_{23} layers for Ag(111). Other theoretical studies of the d_{12} interlayer relaxations for Ag(111) are similarly in the range of -0.03% to -1.86%[72-75] for d_{12}. For d_{23}, the sign of the interlayer change, expansion(+) or contraction(−), varies in the literature, but is generally quite small, less than 0.3% in magnitude.[72,75] Since functionals are known to over or under predict atom–atom spacing, as shown above with the reporting of percent error for bulk metal lattice constant, we assess functionals by comparing the computed ratio of d_{23}/d_{12} interlayer relaxations to the experimentally measured ratio for all surfaces (Table 1). Due to experimental uncertainty, this error was computed without the inclusion of the Ag(111) and Au(111) surface. On this basis, we find that RPBE and RTPSS performed the best.

Metal surface properties: potential of zero charge. Another property of electrochemical interest is the potential of zero charge (PZC) for understanding the effects of the double layer phenomena. The PZC is defined for ideally polarizable surfaces undergoing no charge transfer. Under these conditions, the PZC is the potential at which a metal surface in contact with a
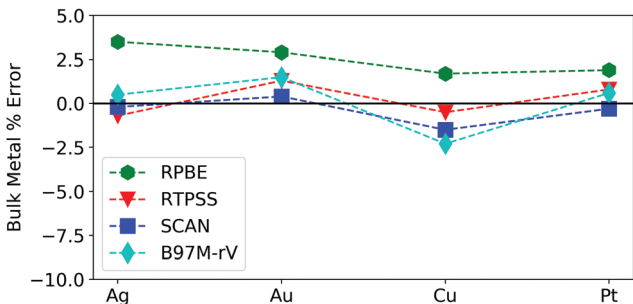

Fig. 3 DFT calculated bulk metal lattice constants compared to experimental values. The raw data is listed in Section S2 of the ESI.†

Table 1 Surface formation energy and surface relaxations for M = Ag, Au, Cu, and Pt. See Fig. 2 for d_{bulk}, d_{12}, and d_{23} distance definitions[80]

		RPBE	RTPSS	SCAN	B97M-rV	Expt.
Ag(110)	d_{bulk} (Å)	1.50	1.45	1.44	1.45	1.44
	d_{12} (Å)	1.31 (−12.5%)	1.35 (−7.5%)	1.30 (−9.6%)	1.44 (−0.7%)	1.33 (−7.6%)[81]
	d_{23} (Å)	1.50 (+0.3%)	1.49 (+2.5%)	1.55 (+7.4%)	1.54 (+5.9%)	1.50 (+4.1%)[81]
	d_{23}/d_{12} (Å)	1.15	1.10	1.19	1.07	1.13
	$2d_{bulk}$ (Å)	2.99	2.91	2.88	2.90	2.89
	d_{13} (Å)	2.81 (−6.1%)	2.84 (−2.5%)	2.85 (−1.1%)	2.97 (+2.6%)	2.79 (−3.5%)[81]
	E_S (eV Å^{-2})	0.04	0.07	0.08	0.07	0.082[68]
Ag(111)	d_{bulk} (Å)	2.44	2.38	2.36	2.37	2.36
	d_{12} (Å)	2.47 (+0.1%)	2.36 (−0.1%)	2.35 (−0.3%)	2.45 (+3.4%)	<−2%,[71] −2.5%[70]
	d_{23} (Å)	2.42 (−0.1%)	2.36 (−0.1%)	2.36 (0.0%)	2.41 (+1.7%)	−0.6%[70]
	d_{23}/d_{12} (Å)	—	—	—	—	—
	$2d_{bulk}$ (Å)	4.89	4.76	4.71	4.74	4.72
	d_{13} (Å)	4.89 (0.0%)	4.71 (−0.1%)	4.70 (−0.1%)	4.86 (+2.6%)	−1.5%
	E_S (eV Å^{-2})	0.03	0.05	0.06	0.07	0.077[68]
Au(111)	d_{bulk} (Å)	2.42	2.39	2.37	2.39	2.36
	d_{12} (Å)	2.45 (+1.2%)	2.41 (+1.0%)	2.39 (+1.2%)	2.48 (+3.8%)	1.5%[82]
	d_{23} (Å)	2.41 (−0.5%)	2.38 (−0.3%)	2.35 (−0.5%)	2.43 (+1.5%)	—
	d_{23}/d_{12} (Å)	—	—	—	—	—
	$2d_{bulk}$ (Å)	4.85	4.77	4.73	4.78	0.7%
	d_{13} (Å)	4.86 (0.3%)	4.79 (+0.3%)	4.75 (+0.3%)	4.91 (+2.7%)	4.71
	E_S (eV Å^{-2})	0.03	0.05	0.05	0.07	0.094[68]
Cu(111)	d_{bulk} (Å)	2.13	2.08	2.06	2.04	2.09
	d_{12} (Å)	2.11 (−0.2%)	2.07 (−0.4%)	2.04 (−0.8%)	2.09 (+2.4%)	2.08 (−0.7%)[83]
	d_{23} (Å)	2.10 (−0.8%)	2.08 (0.0%)	2.05 (−0.3%)	2.08 (+1.9%)	2.08 (−0.6%)[83]
	d_{23}/d_{12} (Å)	1.00	1.00	1.00	1.00	1.00
	$2d_{bulk}$ (Å)	4.25	4.16	4.12	4.08	4.18
	d_{13} (Å)	4.22 (−0.5%)	4.15 (−0.2%)	4.09 (−0.6%)	4.17 (+2.1%)	4.16 (−0.5%)
	E_S (eV Å^{-2})	0.06	0.08	0.09	0.11	0.111[68]
Pt(111)	d_{bulk} (Å)	2.31	2.29	2.26	2.28	2.27
	d_{12} (Å)	2.34 (+1.3%)	2.32 (+1.6%)	2.30 (+1.8%)	2.33 (+2.5%)	2.31 (+1.6%)[84,85]
	d_{23} (Å)	2.29 (−0.8%)	2.28 (−0.3%)	2.25 (−0.4%)	2.29 (+0.7%)	2.27 (0.0%)[84,85]
	d_{23}/d_{12} (Å)	0.98	0.98	0.98	0.98	0.98
	$2d_{bulk}$ (Å)	4.62	4.57	4.52	4.55	4.54
	d_{13} (Å)	4.63 (+0.2%)	4.60 (+0.6%)	4.55 (+0.7%)	4.63 (+1.6%)	4.58 (+0.9%)
	E_S (eV Å^{-2})	0.07	0.09	0.09	0.12	0.155[68]

solution is electrically neutral and has no excess charge. In experimental systems, uncertainty in the PZC can arise due to adsorbed species from the electrolyte or from contaminants that introduce charge transfer to/from the surface. Due to this uncertainty, the potential of zero free charge (PZFC) is differentiated from the potential of zero total charge (PZTC). The PZFC is the potential at which an adsorbate-free electrode surface is neutral, and thus is an intrinsic property of the metal, whereas the PZTC includes the effects of adsorbed surface species.[76–78] We calculated the PZFC and compared it to the experimental results, shown in Fig. 6. The experimental reference potential is commonly the standard hydrogen electrode (SHE). A convenient computational reference potential is the electrostatic potential in the bulk of an electrolyte, as this is zero in an electrolyte that is described by the Poisson–Boltzmann equation, which we evaluated with VASPsol.[79] To compare the calculated PZC to the experimentally measured PZC, a computational SHE voltage would then be calculated and used as a reference. However, we note that this procedure would shift the predicted potentials (since the current reference potential is in the electrolyte and is 0V); therefore, we have not included the SHE. Instead, we show the calculated PZC value correlated with the

experimentally measured PZC in Fig. 6. For RPBE and RTPSS the PZTC is under predicted, while SCAN over predicts the PZTC, and B97M-rV both under and over predicts the value.

Summary for bulk and bare surface properties. Fig. 7 summarizes the metal and surface properties predicted by each functional as measured by the mean relative error percent for each property, n, averaged over all metals, m:

$$MRE\% = \text{Average}\left(\frac{n_{m,\text{theory}} - n_{m,\text{exp}}}{n_{m,\text{exp}}}\right). \quad (3)$$

The RTPSS functional performs best overall for the bulk and surface metal properties examined here. RPBE and B97M-rV track fairly consistently for errors, with the exception of surface layer relaxations, where their absolute value of error is commensurate but the sign inverted. SCAN is primarily dominated by larger errors in surface energy and PZFC trends and RPBE and B97M-rV dominated by large errors in the interlayer relaxations.

3.2 Properties of free and adsorbed CO on metal surfaces

Free CO properties. The equilibrium bond length and vibrational frequency for the free CO molecule were calculated for each functional using VASP (Fig. S2, ESI†). The error for the
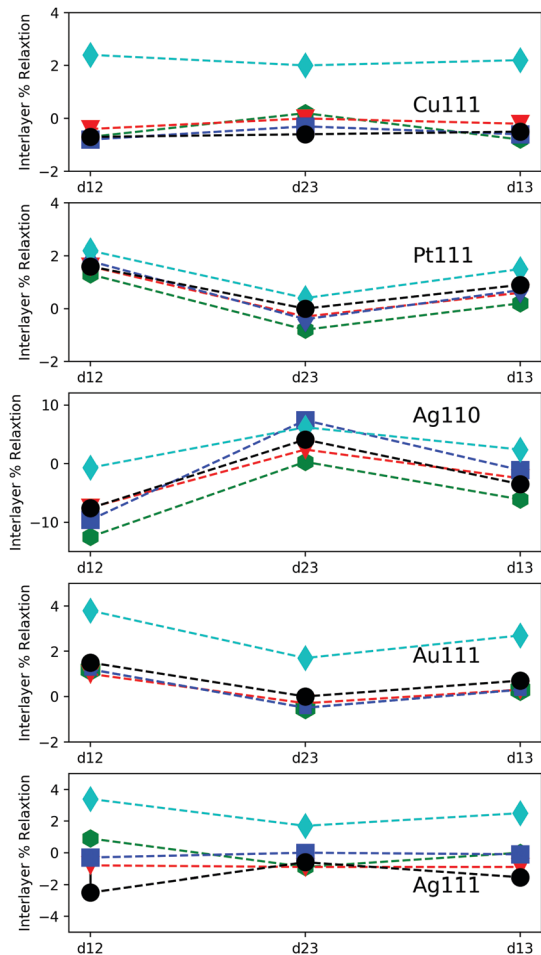
Fig. 5 DFT calculated interlayer relaxations for all metal surfaces compared to experimental values. Data is reported in Table 1. RPBE results are reported as green hexagons, RTPSS as red triangles, B97MrV as teal diamonds, SCAN as blue squares, and experiment, where available, is in black circles.
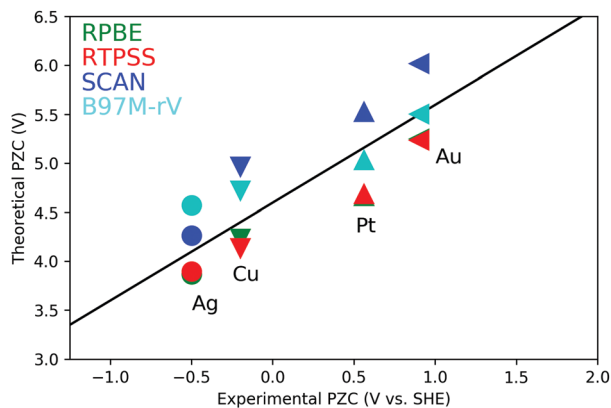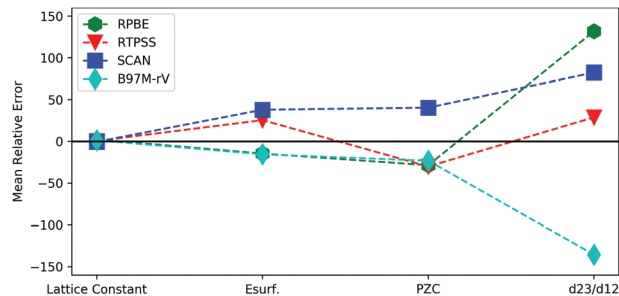

Fig. 7 Mean relative error for each functional. Lattice constant is the bulk metal lattice constant, $E_{surf.}$ is the energy of formation for the surface, PZTC is the potential of zero charge, and d_{23}/d_{12} is the ratio of the d_{23} to the d_{12} interlayer spacings.

0.3%. RPBE and RTPSS were both under 2% error, with RPBE at 1.8% and RTPSS at 1.4%. The DFT calculated harmonic vibrational frequencies were compared to the experimental value of 2169 cm^{-1}.[87,88] The errors for SCAN, B97M-rV, RTPSS, and RPBE were 0.8%, 2.6%, −2.3%, and −3.2%, respectively.

Energetics of adsorbed CO on metal surfaces. Many GGA and meta-GGA functionals such as PBE,[89] PBEsol,[90] TPSS,[91] revTPSS,[92] SCAN,[44] and PW91[31,35,41] are known to overestimate chemisorption energies, the so called "over-binding problem". Some functionals have been explicitly corrected for over-binding, such as RPBE,[33] a modified version of PBE. By design, RPBE therefore performs well for strongly bound molecules at surfaces.[35] Similarly, RTPSS[41] is a modified TPSS functional and shows similar improvement in the magnitude of adsorption energy.

The theoretical and experimental adsorption energies for CO on each metal surface are shown in Fig. 8 for all tested functionals. The experimental trend for the strength of CO
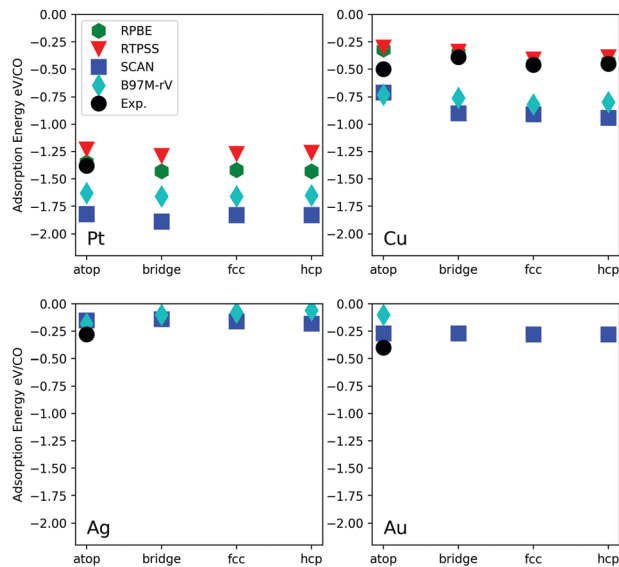

Fig. 6 Theoretical vs. experimental PZC for 111 surfaces of Au, Ag, Pt, and Cu.

Fig. 8 DFT calculated adsorption energies for CO on M = Pt, Cu, Au, and Ag compared to experimentally observed adsorption energies, where available.

calculated equilibrium bond length compared to the experimental value of 1.13 Å[86] was as follows: SCAN and B97M-rV were both under 1% error, with SCAN at 0.6% and B97M-rV at

adsorption to the (111) metal surfaces is Ag[53,55] ∼ Au[54,55] < Cu[93] < Pt.[35,94] For the stronger binding metals, Cu and Pt, RPBE and RTPSS produce the correct magnitude of the adsorption energies. However, both SCAN and B97M-rV, which have not been explicitly corrected for the over-binding problem, overbind CO on Cu and Pt.

For the weaker binding metal surfaces, Au and Ag, no energetically stable binding states could be identified with RTPSS, nor with RPBE. By contrast, SCAN and B97M-rV predicted energetically stable binding states, in the same range as the adsorption energy found experimentally, consistent with previous findings.[95] Although SCAN does include some intermediate range dispersion, it does not include the true long range dispersion that B97M-rV does, and SCAN (as well as RPBE) have therefore been found to perform poorly for intermolecular interactions.[10] Further illustration of the importance of long range dispersion is apparent when the rVV10 non-local interaction is added to SCAN, in which case the functional performs well for surface relaxations and adsorption of benzene to metal surfaces.[45]

Site preference for adsorbed CO on metal surfaces. The experimentally observed lowest energy adsorption site on the (111) surfaces of Au, Ag, Cu, and Pt is the atop site.[35,53–55,93,94] It is well-known that semi-local GGAs fail to accurately reproduce the experimentally observed adsorption site preference,[36,96] which suggests that such functionals do not properly capture the interactions between the adsorbate, CO, and the metal. One issue is that semi-local GGA functionals do not accurately align the HOMO and LUMO levels of CO with respect to the metal Fermi level.[96,97] In addition, the HOMO–LUMO gap in the adsorbate can be underestimated due to self-interaction errors,[98] which may lead to the computed energetic preference for two- and three-fold coordination environments over the experimentally observed singly coordinated sites.[99] Many possible solutions[94,96,97,100–104] have been suggested for this problem, of varying success and computational complexity. This drawback has been thoroughly studied for CO on various metal surfaces, with Pt(111) probably the most well characterized.[31,34,37,96] CO is found experimentally to adsorb on the atop site of a Pt(111) surface, semi-local GGA DFT calculations at 0 K predict the two-fold or three-fold adsorption sites to be preferred. The effects of temperature on this site preference will be investigated in a future publication.[105] Likewise, experiments for CO adsorption on a Rh(111),[100] and Ag(111) and Au(111)[94,103] show that CO prefers to adsorb at the atop sites, whereas theory predicts CO to adsorb at multi-coordinated sites.

In Table 2, the preferred adsorption site is shown in bold. For the strongly binding metals, Pt and Cu, all functionals examined herein predicted a preference for a multi-coordinated sites over the atop site. For the weakly binding metals, only SCAN and B97M-rV predicted adsorption. SCAN predicted multi-coordinated site preference over the atop site, however B97M-rV correctly predicted the atop site to be preferred on Ag(111) and Au(111). We note that RTPSS has previously been reported to predict preferred adsorption at the atop site,[41] but we were not able to reproduce this result and believe it is due to differences in bulk atom spacing used here *versus* the earlier theoretical work. For the Cu(111) surface, the experimental

Table 2 Adsorbate site preference DFT predictions compared to experimental adsorption energies, where available, for Pt(111)(top) and Cu(111)(bottom). The DFT predicted preferred site is in bold. The last row represent the energy difference between the most stable and least stable sites

	RPBE	RTPSS	SCAN	B97M-rV	Exp.
Pt(111)					
Atop	−1.35	−1.23	−1.82	−1.63	−1.38
Bridge	**−1.43**	**−1.29**	**−1.89**	**−1.66**	—
Fcc	−1.42	−1.27	−1.83	**−1.66**	—
Hcp	**−1.43**	−1.26	−1.83	−1.65	—
E range	0.08	0.06	0.07	0.03	—
Cu(111)					
Atop	−0.32	−0.30	−0.72	−0.73	−0.50
Bridge	−0.35	−0.34	−0.93	−0.76	−0.39
Fcc	**−0.45**	**−0.41**	−0.94	**−0.82**	−0.46
Hcp	−0.43	−0.39	**−0.96**	−0.80	−0.45
E range	0.13	0.11	0.24	0.09	0.11
Ag(111)					
Atop	—	—	−0.15	**−0.18**	−0.28
Bridge	—	—	−0.14	−0.13	—
Fcc	—	—	−0.16	−0.13	—
Hcp	—	—	**−0.18**	−0.13	—
E range	—	—	0.04	0.05	—
Au(111)					
Atop	—	—	−0.27	**−0.15**	−0.4
Bridge	—	—	−0.27	—	—
Fcc	—	—	**−0.28**	—	—
Hcp	—	—	**−0.28**	—	—
E range	—	—	0.01	0.15	—

range of adsorption energies between that for multi-coordinated sites and that for the atop site is 0.11 eV/CO or 2.5 kcal mol⁻¹, which is a small energy span. A similar range of adsorption energies is calculated for CO adsorption on Cu(111), 0.13 eV/CO, 0.11 eV/CO, 0.24 eV/CO, and 0.09 eV/CO for RPBE, RTPSS, SCAN, and B97MrV, respectively. Given that adsorption site preference for DFT functionals has historically been wrong, it is promising that B97M-rV correctly predicts the atop adsorption site as the preferred site on Au and Ag. While it is troublesome that the adsorption trends cannot be predicted correctly for the other metal surfaces for all functionals, the calculated energy range for the different adsorption sites can be leveraged as a range of uncertainty for theoretical predictions of CO reduction pathways. This suggests that competing species in a predicted CO2RR pathway that have calculated energy differences less than the difference between a multi-coordinated site and the atop site cannot be meaningfully differentiated.

Vibrational frequencies for adsorbed CO on metal surfaces. Finally, we consider the vibrational frequencies for CO on M = Au, Ag, Cu, and Pt. The equilibrium bond lengths and harmonic vibrational frequencies for the CO molecule are shown in Section S2 of the ESI† for each functional compared to the experimental equilibrium bond length and harmonic vibrational frequency.[86] The black data points in Fig. 9 show the difference between the experimentally observed C–O stretching frequency, where the data are available, and the vibrational frequency for CO in the gas phase. The vibrational frequency trends for CO on Pt and Cu follow the experimental trends of atop at 1990–2100 cm⁻¹, bridge at 1830–1880 cm⁻¹, and hollow at 1750–1810 cm⁻¹.[94,96]
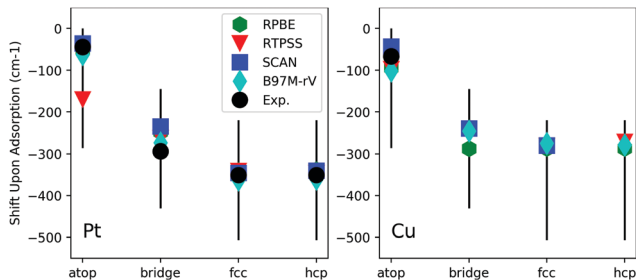
Fig. 9 DFT calculated changes in harmonic vibrational frequency for CO from gas phase to adsorption at the atop, bridge, fcc, or hcp sites on the (111) surfaces of M = Pt and Cu.

The corresponding frequency shifts with respect to the gas phase for CO on metals as follows: 400–475 cm^{-1}, 340–380 cm^{-1}, and 300–350 cm^{-1} for the atop, bridge, and hollow sites, respectively.[96] The CO stretching frequency generally decreases with increasing coordination on metal surfaces. This observation is commonly used to identify adsorption site by IR frequency.[94,96]

The change in frequency for CO upon surface adsorption is shown in Fig. 9. For Pt, the red shifts calculated in the harmonic approximation using the RPBE, SCAN, and B97M-rV functionals are in good agreement with those seen experimentally, whereas RTPSS predicts higher red shifts for CO adsorbed in the atop position than observed experimentally. For Cu, RPBE and RTPSS predict comparable red shifts and both predictions are larger than what is observed experimentally, whereas SCAN predicts a lower shift than is seen experimentally. Part of the deviations between computation and experiment is likely due to the harmonic approximation.

Summary for metal–adsorbate surface interactions. The mean relative errors in predicting the properties of molecular CO and of CO adsorbed on to Ag, Au, Cu, and Pt are presented in Fig. 10 for each functional. The MREs for the prediction of the bond length and vibrational frequency of adsorbed CO are small for all functionals. While SCAN is able to reproduce the magnitude of the adsorption energies for Au and Ag surfaces accurately, this functional leads to very large errors for the stronger binding metals, Cu and Pt. The scenario is similar for B97M-rV, which is analogously able to reproduce the magnitude of adsorption energetics for Au and Ag but overbinds Cu and Pt,
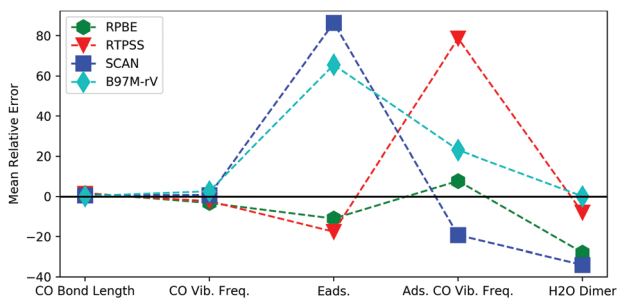
leading to large errors for this functional. This behavior is expected for local/semi-local DFT. RPBE and RTPSS are both corrected for overbinding and as a result suffer from lessened adsorption energetic errors in Fig. 10. CO frequency shifts upon adsorption for the atop site of Cu(111), and all sites for Pt(111)[96] are best predicted by RPBE at 8%, SCAN and B97M-rV perform similarly at −19% and 23% error, respectively. RTPSS performs more poorly (78%) due primarily to the poor agreement for the atop site on Pt(111).

3.3 Further insights from related molecular systems

The preceding data provide insight into the performance of DFT for modeling the interaction of CO with a metal surface. Nevertheless, the complexity of these systems limits our ability to provide robust computational benchmarks, because such systems are too large to be treated with the systematically reliable computational methods from wave function theory, and there are ambiguities in comparing with experiment. However, this difficulty is not present for molecular metal monocarbonyls (MCOs). We therefore report comparison of density functionals against wave function theory benchmarks for MCOs corresponding to the metal surfaces of present interest (M = Cu, Ag, Au, and Pt). The work here follows previous work of some of us, which addresses the importance[106–108] of charge-transfer in metal–carbonyl interactions.[57] Here, we also consider water–water and water–CO interactions, as a prerequisite for balanced treatment of the solid liquid interface. We compare B97M-rV, RPBE, and SCAN results to those computed using both CCSD(T) and ωB97X-V, a range-separated hybrid GGA[109] previously shown to perform well against experiment for a broad range of MCOs.[57]

Focusing first on the binding energies, Fig. 11 presents a comparison of B97M-rV, RPBE, and SCAN results against CCSD(T) benchmarks, as well as the conventional PBE functional. The best agreement with the benchmark is obtained with B97M-rV, which shows good performance for both weak and strong-binding metal atoms. By contrast, SCAN and PBE exhibit strong overbinding, while RPBE is significantly better. Turning to a broader range of properties, we compare MCO geometries, binding energies, and harmonic vibrational frequencies in Fig. 12 and Tables S2–S4 in the ESI,† respectively. The results for M–C bond lengths of these complexes (Fig. 12(d))

Fig. 10 Mean relative error for each functional. $E_{ads.}$ is the energy of adsorption for the CO molecule and 'Vib. Frequency' is the shift in the adsorbed CO vibrational frequency, both on the metal surface.
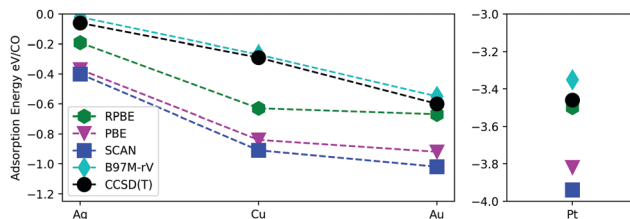

Fig. 11 DFT calculated adsorption energies for CO on single metal atoms (Ag, Cu, Au, and Pt) compared to benchmark CCSD(T) results. The B97MrV functional performs best on this assessment, while PBE and SCAN show most overbinding.
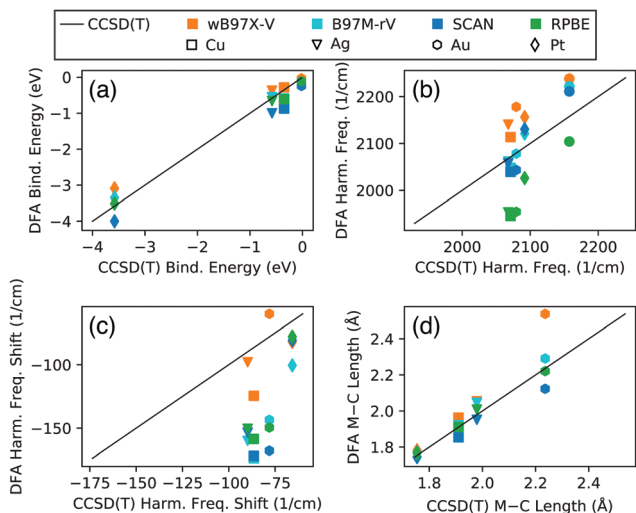
Fig. 12 Benchmark data for metal monocarbonyls (MCOs, M = Cu, Ag, Au, Pt) computed using the Q-Chem package.[56] Results from DFT computations are compared to reference CCSD(T) values for (a) complex binding energies, (b) harmonic frequencies, (c) harmonic frequency shifts relative to isolated CO, and (d) M−C bond lengths. Harmonic frequencies for isolated CO are indicated by the circles in plot (b). Shapes and colors for data points correspond to the M and the method of computation, respectively, as indicated in the legend. See text for computational details.

are broadly similar to the binding energies. Specifically, SCAN is seen to overbind the complexes, while B97M-rV and RPBE provide satisfactory results.

We further benchmark these methods using both the absolute CO harmonic frequency in MCOs and the shift in this frequency upon complex formation (Fig. 12(b) and (c), respectively). The performance differences in these two observables are interesting: B97M-rV and SCAN achieve the best agreement with CCSD(T) in terms of the absolute frequencies, but ωB97X-V is the only functional in this set that reproduces CCSD(T) frequency shifts with any fidelity. We understand these conflicting results in reference to the harmonic frequency of isolated CO predicted by each functional, indicated by the circles in 12(b). The agreement that B97M-rV and SCAN achieve with CCSD(T) for absolute MC−O frequencies is inconsistent with their predictions for isolated CO, which are blue-shifted by over 50 cm^{-1} relative to CCSD(T). We note that the calculated CCSD(T) frequency for CO (2157 cm^{-1}) agrees with the experimentally observed harmonic value of 2170 cm^{-1} to 13 cm^{-1}. The ωB97X-V absolute frequencies, however, are more-or-less consistently blue-shifted relative to CCSD(T), rendering agreement in the frequency shifts exceptional (Fig. 12(c)). By either metric, the RPBE CO frequencies are significantly red-shifted relative to CCSD(T).

It should be noted here that a previous study by some of us[57] indicated that ωB97X-V and CCSD(T) geometries, binding energies, and harmonic CO frequency shifts compared favorably with experimental results across a series of 17 different MCOs. Hence, the agreement between results from RPBE and B97M-rV with those from CCSD(T), particularly in binding energy predictions, is quite promising. Still, the failure of these two functionals to provide

Table 3 Calculated binding energies for the water−CO dimer, computed using geometries from a previous benchmark study of this system.[111] Energies are reported in units of cm^{-1} and percent errors are relative to the value of −646.1 cm^{-1} reported previously[111]

Species	Method	Binding energy	Percent error (%)
H$_2$O−CO	ωB97X-V	−627.5	2.9
	B97M-rV	−674.1	−4.3
	RPBE	−456.0	29.4
	SCAN	−592.6	8.3

accurate CO harmonic frequency shifts illustrates that neither can be viewed as performing ideally.

Solution effects at the electrochemical interface have shown to be important to the overall performance of CO2R fuel cells. Some studies have included these effects with implicit water, but there also exists the possibility of utilizing explicit water in MD-DFT simulations. To this end, we have assessed the ability of the functionals examined to capture the H$_2$O dimerization energy from the S22[110] molecular DFT benchmark dataset. We found B97M-rV, RPBE, SCAN, and RTPSS to perform at <0.2%, −28%, 8%, and −34% errors compared to the CCSD(T) benchmark computed previously[110] and found here to be −0.22 eV.

Similarly, water–CO interactions must be treated consistently with water–water interactions, and M–CO interactions to describe the solid–liquid interface with adequate fidelity. A recent study of the water–CO potential energy surface reports a benchmark binding energy of −646.1 cm^{-1} for this system.[111] Using the global minimum structure from this work and analogous computational procedures (see Section S3 of the ESI† for details), we find that B97M-rV, SCAN, and RPBE reproduce the water–CO dimer binding energy with −4%, 8%, and 29% errors, respectively (Table 3). For reference, higher-level ωB97X-V computations yield a 3% error, only marginally better than the B97M-rV result. Both RPBE and SCAN overbind the water–CO dimer. Taken in conjunction with the binding energies for the water dimer in the preceding paragraph, and the M–CO systems, these data indicate that B97M-rV is the most balanced of the functionals considered for these molecular properties, achieving moderate to high fidelity in reproducing benchmark binding energies for all of the relevant molecular systems.
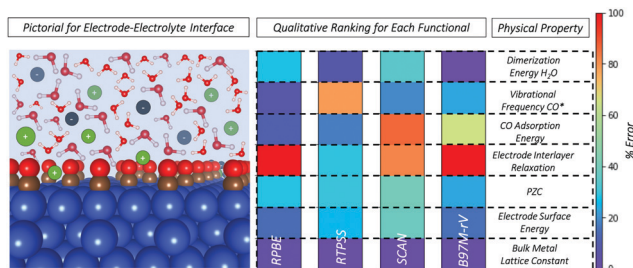

Fig. 13 Qualitatively ranked efficacy for each functional for each property assessed herein. Ranking quantitative and is the absolute value for the error reported in Fig. 7 and 10. The ranking bar on the right hand side of the figure, ranging from 0–100% error, shows that "cool" colors are low error while "warm colors" are high error.

4. Conclusions

We have presented a benchmark study of bulk and interfacial properties for five metal surfaces with four DFT functionals whose results are ranked quantitatively in Fig. 13. The ranking is based on errors reported in Fig. 7 and 10. "Cool" colors are low error percent and "warm"" colors are high error percent, as shown in the error bar color code on the right of Fig. 13. These analyses stand as a framework upon which an electrochemical model can be built and potential energy descriptors for CO reduction could be identified. Our explicit conclusions for each investigated property assessed herein are as follows:

Bulk metal and bare surface properties

When the absolute average errors are presented for all properties taken together, RTPSS consistently performed the best for the metal properties assessed herein.

Binding energetics

For the weakly binding surfaces, Ag and Au, we find that SCAN and B97M-rV adequately represent the magnitude of the experimental binding energy for the atop site. B97M-rV performed very well compared to CCSD(T) benchmarks for molecular metal carbonyl systems. For intermediate binding energy motifs represented by the water dimer, B97M-rV is as accurate as the CCSD(T) benchmark while SCAN manifests small amounts of overbinding, and RPBE and RTPSS reproduce the water–water binding energy quite poorly. For the strongly binding interactions represented by the CO adsorbate on Cu and Pt surfaces, we find that SCAN and B97M-rV excessively overbinds, indicating that the overbinding problem has not been overcome with this new meta-GGA functional. We find that RPBE and RTPSS do not overbind, as expected since they were explicitly corrected for overbinding. We caution that the surface binding energy calculations are under static conditions and at 0 K. Thermal effects can influence energetic stability and calculated properties, and will be assessed in a separate forthcoming study.

Site-preference for binding and vibrational frequencies

All functionals inaccurately predicted a multi-coordinated site as the preferred binding site for CO on Pt(111) and Cu(111). Encouragingly, the correct site is predicted by B97M-rV on Ag(111) and Au(111). We recommend that the energy difference between the multi-coordinated site and the atop site be utilized as an energy range, outside which, no energetic preference predictions should be made. This is especially relevant to the development of microkinetic models for CO_2 reduction, which take DFT energies as inputs. We also emphasize that this energetic preference error for semi-local DFT is due to incorrect estimation of the HOMO–LUMO gap for CO and alignment of these levels with the energy band of the metal. Compared to the experimental frequency shifts, RPBE, B97M-rV and SCAN outperform RTPSS on the limited experimental data set for CO bound on metal surfaces. We note that anharmonic effects on vibrational frequency shifts may affect the comparison of harmonic calculations with experimental values. The results for

molecular monocarbonyls (Section 3.3) qualify these trends, indicating that none of these functionals yield high quality CO frequency shifts with consistency. Additionally, these latter results suggest that any agreement in absolute CO frequencies obtained by these functionals is fortuitous, and due to inconsistencies in their treatment of gas-phase CO.

The aim of this study was to investigate the accuracy of DFT functionals for their ability to determine properties at the metal–adsorbate interface in order to highlight strengths, shortcomings, and make recommendations for computational methodologies to be utilized in more complete solid–liquid interface models. With this in mind, RPBE remains a reliable GGA functional (with comparable accuracy but a lower cost than the meta-GGA functionals) for characterizing the bulk metal or surface properties of metals for which it was designed. However, an indicator for problems ahead is the failure of RPBE to describe the solid–liquid interface, as is manifest in something as basic as the water dimer for which it performs poorly. Similarly, SCAN also performed poorly for the water dimerization energy.

Generally, RTPSS and B97M-rV performed the best for the water dimerization energy, while both having strengths and weaknesses at capturing the metal–adsorbate interaction. For interactions with the surface, RTPSS performed well for strongly binding metals where B97M-rV suffered from the overbinding problem. However, for the weaker binding metals, RTPSS predicted no adsorption and B97M-rV was able to capture the appropriate site preference for CO on Au and Ag. Due to this, we recommend both RTPSS and B97M-rV due to their abilities to treat molecular interactions accurately. For systems where strong metal–adsorbate interactions are expected, RTPSS is a good choice. For systems ruled by weaker metal–adsorbate interactions, B97M-rV is a good choice. It is also evident that there remains considerable scope for improvement in the performance of functionals; it is an interesting open question how much more can be accomplished at the meta-GGA level.

Conflicts of interest

MHG is a part-owner of Q-Chem Inc.

Acknowledgements

References

1 Z. He, T. Liu, J. Tang, C. Zhou, L. Wen, J. Chen and S. Song, *Electrochim. Acta*, 2016, **222**, 1234–1242.

2 W. J. Durand, A. A. Peterson, F. Studt, F. Abild-Pedersen and J. K. Nørskov, *Surf. Sci.*, 2011, **605**, 1354–1359.

3 N. Hoshi, M. Kato and Y. Hori, *J. Electroanal. Chem.*, 1997, **440**, 283–286.

4 Q. Lu, J. Rosen, Y. Zhou, G. S. Hutchings, Y. C. Kimmel, J. G. Chen and F. Jiao, *Nat. Commun.*, 2014, **5**, 1–6.

5 J. P. Jones, G. K. Prakash and G. A. Olah, *Isr. J. Chem.*, 2014, **54**, 1451–1466.

6 J. Resasco, L. D. Chen, E. Clark, C. Tsai, C. Hahn, T. F. Jaramillo, K. Chan and A. T. Bell, *J. Am. Chem. Soc.*, 2017, **139**, 11277–11287.

7 S. Ringe, E. L. Clark, J. Resasco, A. Walton, B. Seger, A. T. Bell and K. Chan, *Energy Environ. Sci.*, 2019, 17–25.

8 M. R. Singh, J. D. Goodpaster, A. Z. Weber, M. Head-Gordon and A. T. Bell, *Proc. Natl. Acad. Sci. U. S. A.*, 2017, **114**, E8812–E8821.

9 A. Krylov, T. L. Windus, T. Barnes, E. Marin-Rimoldi, J. A. Nash, B. Pritchard, D. G. A. Smith, D. Altarawy, P. Saxe, C. Clementi, T. D. Crawford, R. J. Harrison, S. Jha, V. S. Pande and T. Head-Gordon, *J. Chem. Phys.*, 2018, **149**, 180901.

10 N. Mardirossian and M. Head-Gordon, *Mol. Phys.*, 2017, **115**, 2315–2372.

11 J. A. Gauthier, S. Ringe, C. F. Dickens, A. J. Garza, A. T. Bell, M. Head-Gordon, J. K. Nørskov and K. Chan, *ACS Catal.*, 2019, **9**, 920–931.

12 S. Ringe, H. Oberhofer, C. Hille, S. Matera and K. Reuter, *J. Chem. Theory Comput.*, 2016, **12**, 4052–4066.

13 Y. Ping, R. J. Nielsen and W. A. Goddard, *J. Am. Chem. Soc.*, 2017, **139**, 149–155.

14 J. D. Goodpaster, A. T. Bell and M. Head-Gordon, *J. Phys. Chem. Lett.*, 2016, **7**, 1471–1477.

15 T. Ludwig, J. A. Gauthier, K. S. Brown, S. Ringe, J. K. Nørskov and K. Chan, *J. Phys. Chem. C*, 2019, **123**, 5999–6009.

16 X. Liu, P. Schlexer, J. Xiao, Y. Ji, L. Wang, R. B. Sandberg, M. Tang, K. S. Brown, H. Peng, S. Ringe, C. Hahn, T. F. Jaramillo, J. K. Nørskov and K. Chan, *Nat. Commun.*, 2019, **10**, 1–10.

17 E. Skúlason, G. S. Karlberg, J. Rossmeisl, T. Bligaard, J. Greeley, H. Jónsson and J. K. Nørskov, *Phys. Chem. Chem. Phys.*, 2007, **9**, 3241–3250.

18 J. Gauthier, C. Dickens, S. Ringe and K. Chan, *ChemPhysChem*, 2019, 1–8.

19 S. Sakong and A. Groß, *ACS Catal.*, 2016, **6**, 5575–5586.

20 T. Cheng, H. Xiao and W. A. Goddard, *Proc. Natl. Acad. Sci. U. S. A.*, 2017, **114**, 1795–1800.

21 S. N. Steinmann, C. Michel, R. Schwiedernoch and P. Sautet, *Phys. Chem. Chem. Phys.*, 2015, **17**, 13949–13963.

22 A. Garza, A. T. Bell and M. Head-Gordon, *ACS Catal.*, 2018, **8**(2), 1490–1499.

23 C. D. Taylor, S. A. Wasileski, J. S. Filhol and M. Neurock, *Phys. Rev. B: Condens. Matter Mater. Phys.*, 2006, **73**, 1–16.

24 J. S. Filhol and M. Neurock, *Angew. Chem., Int. Ed.*, 2006, **45**, 403–406.

25 A. D. Dutoi and M. Head-Gordon, *Chem. Phys. Lett.*, 2006, **422**, 230–233.

26 T. Bally and G. N. Sastry, *J. Phys. Chem. A*, 1997, **101**, 7923–7925.

27 A. Ruzsinszky, J. P. Perdew, G. I. Csonka, O. A. Vydrov and G. E. Scuseria, *J. Chem. Phys.*, 2006, **125**, 1–8.

28 A. Ruzsinszky, J. P. Perdew, G. I. Csonka, O. A. Vydrov and G. E. Scuseria, *J. Chem. Phys.*, 2007, **126**, 1–8.

29 S. Mallikarjun Sharada, T. Bligaard, A. C. Luntz, G.-J. Kroes and J. K. Nørskov, *J. Phys. Chem. C*, 2017, **121**, 19807–19815.

30 B. G. Johnson, C. A. Gonzales, P. M. Gill and J. A. Pople, *Chem. Phys. Lett.*, 1994, **221**, 100–108.

31 L. Schimka, J. Harl, A. Stroppa, A. Grüneis, M. Marsman, F. Mittendorfer and G. Kresse, *Nat. Mater.*, 2010, **9**, 741–744.

32 V. I. Anisimov, J. Zaanen and O. K. Andersen, *Phys. Rev. B: Condens. Matter Mater. Phys.*, 1991, **44**, 943–954.

33 B. Hammer, L. B. Hansen and J. K. Nørskov, *Phys. Rev. B: Condens. Matter Mater. Phys.*, 1999, **59**, 7413–7421.

34 P. J. Feibelman, B. Hammer, J. K. Nørskov, F. Wagner, M. Scheffler, R. Stumpf, R. Watwe and J. Dumesic, *J. Phys. Chem. B*, 2001, **105**, 4018–4025.

35 J. Wellendorff, T. L. Silbaugh, D. Garcia-Pintos, J. K. Nørskov, T. Bligaard, F. Studt and C. T. Campbell, *Surf. Sci.*, 2015, **640**, 36–44.

36 Q. Zhao and H. J. Kulik, *J. Phys. Chem. Lett.*, 2019, **10**, 5090–5098.

37 A. Stroppa and G. Kresse, *New J. Phys.*, 2008, **10**, 063020.

38 A. J. Cohen, P. Mori-Sánchez and W. Yang, *Science*, 2008, **321**, 792–794.

39 A. J. Cohen, P. Mori-Sánchez and W. Yang, *Phys. Rev. B: Condens. Matter Mater. Phys.*, 2008, **77**, 1–6.

40 A. J. Cohen, P. Mori-Sánchez and W. Yang, *Chem. Rev.*, 2012, **112**, 289–320.

41 A. J. Garza, A. T. Bell and M. Head-Gordon, *J. Chem. Theory Comput.*, 2018, **14**, 3083–3090.

42 N. Mardirossian and M. Head-Gordon, *J. Chem. Phys.*, 2015, **142**, 074111.

43 N. Mardirossian, L. Ruiz Pestana, J. C. Womack, C. K. Skylaris, T. Head-Gordon and M. Head-Gordon, *J. Phys. Chem. Lett.*, 2017, **8**, 35–40.

44 J. Sun, A. Ruzsinszky and J. Perdew, *Phys. Rev. Lett.*, 2015, **115**, 1–6.

45 H. Peng, Z.-H. Yang, J. P. Perdew and J. Sun, *Phys. Rev. X*, 2016, **6**, 041005.

46 J. Qiao, Y. Liu, F. Hong and J. Zhang, *Chem. Soc. Rev.*, 2014, **43**, 631–675.

47 Y. Hori, *Handbook of Fuel Cells*, John Wiley & Sons, Ltd, Chichester, UK, 2010, pp. 1–14.

48 Z. P. Jovanov, H. A. Hansen, A. S. Varela, P. Malacrida, A. A. Peterson, J. K. Nørskov, I. E. Stephens and I. Chorkendorff, *J. Catal.*, 2016, **343**, 215–231.

49 J. Sun, M. Marsman, A. Ruzsinszky, G. Kresse and J. P. Perdew, *Phys. Rev. B: Condens. Matter Mater. Phys.*, 2011, **83**, 2–5.

50 G. Kresse and J. Furthmüller, *Phys. Rev. B: Condens. Matter Mater. Phys.*, 1996, **54**, 11169–11186.

51 P. E. Blöchl, *Phys. Rev. B: Condens. Matter Mater. Phys.*, 1994, **50**, 17953–17979.

52 M. Methfessel and A. T. Paxton, *Phys. Rev. B: Condens. Matter Mater. Phys.*, 1989, **40**, 3616–3621.

53 G. McElhiney, H. Papp and J. Pritchard, *Surf. Sci.*, 1976, **54**, 617–634.

54 D. P. Engelhart, R. J. Wagner, A. Meling, A. M. Wodtke and T. Schäfer, *Surf. Sci.*, 2016, **650**, 11–16.

55 T. L. Silbaugh and C. T. Campbell, *J. Phys. Chem. C*, 2016, **120**, 25161–25172.

56 Y. Shao, Z. Gan, E. Epifanovsky, A. T. Gilbert, M. Wormit, J. Kussmann, A. W. Lange, A. Behn, J. Deng, X. Feng, D. Ghosh, M. Goldey, P. R. Horn, L. D. Jacobson, I. Kaliman, R. Z. Khaliullin, T. Kuś, A. Landau, J. Liu, E. I. Proynov, Y. M. Rhee, R. M. Richard, M. A. Rohrdanz, R. P. Steele, E. J. Sundstrom, H. L. Woodcock, P. M. Zimmerman, D. Zuev, B. Albrecht, E. Alguire, B. Austin, G. J. O. Beran, Y. A. Bernard, E. Berquist, K. Brandhorst, K. B. Bravaya, S. T. Brown, D. Casanova, C.-M. Chang, Y. Chen, S. H. Chien, K. D. Closser, D. L. Crittenden, M. Diedenhofen, R. A. DiStasio, H. Do, A. D. Dutoi, R. G. Edgar, S. Fatehi, L. Fusti-Molnar, A. Ghysels, A. Golubeva-Zadorozhnaya, J. Gomes, M. W. Hanson-Heine, P. H. Harbach, A. W. Hauser, E. G. Hohenstein, Z. C. Holden, T.-C. Jagau, H. Ji, B. Kaduk, K. Khistyaev, J. Kim, J. Kim, R. A. King, P. Klunzinger, D. Kosenkov, T. Kowalczyk, C. M. Krauter, K. U. Lao, A. D. Laurent, K. V. Lawler, S. V. Levchenko, C. Y. Lin, F. Liu, E. Livshits, R. C. Lochan, A. Luenser, P. Manohar, S. F. Manzer, S.-P. Mao, N. Mardirossian, A. V. Marenich, S. A. Maurer, N. J. Mayhall, E. Neuscamman, C. M. Oana, R. Olivares-Amaya, D. P. O'Neill, J. A. Parkhill, T. M. Perrine, R. Peverati, A. Prociuk, D. R. Rehn, E. Rosta, N. J. Russ, S. M. Sharada, S. Sharma, D. W. Small, A. Sodt, T. Stein, D. Stück, Y.-C. Su, A. J. Thom, T. Tsuchimochi, V. Vanovschi, L. Vogt, O. Vydrov, T. Wang, M. A. Watson, J. Wenzel, A. White, C. F. Williams, J. Yang, S. Yeganeh, S. R. Yost, Z.-Q. You, I. Y. Zhang, X. Zhang, Y. Zhao, B. R. Brooks, G. K. Chan, D. M. Chipman, C. J. Cramer, W. A. Goddard, M. S. Gordon, W. J. Hehre, A. Klamt, H. F. Schaefer, M. W. Schmidt, C. D. Sherrill, D. G. Truhlar, A. Warshel, X. Xu, A. Aspuru-Guzik, R. Baer, A. T. Bell, N. A. Besley, J.-D. Chai, A. Dreuw, B. D. Dunietz, T. R. Furlani, S. R. Gwaltney, C.-P. Hsu, Y. Jung, J. Kong, D. S. Lambrecht, W. Liang, C. Ochsenfeld, V. A. Rassolov, L. V. Slipchenko, J. E. Subotnik, T. Van Voorhis, J. M. Herbert, A. I. Krylov, P. M. Gill and M. Head-Gordon, *Mol. Phys.*, 2015, **113**, 184–215.

57 E. Rossomme, C. N. Lininger, A. T. Bell, T. Head-Gordon and M. Head-Gordon, *Phys. Chem. Chem. Phys.*, 2020, **22**, 781–798.

58 N. Mardirossian and M. Head-Gordon, *Phys. Chem. Chem. Phys.*, 2014, **16**, 9904–9924.

59 K. Raghavachari, G. W. Trucks, J. A. Pople and M. Head-Gordon, *Chem. Phys. Lett.*, 1989, **157**, 479–483.

60 D. Rappoport and F. Furche, *J. Chem. Phys.*, 2010, **133**, 134105.

61 F. Weigend and R. Ahlrichs, *Phys. Chem. Chem. Phys.*, 2005, **7**, 3297–3305.

62 F. Weigend, F. Furche and R. Ahlrichs, *J. Chem. Phys.*, 2003, **119**, 12753–12762.

63 S. P. Ong, W. D. Richards, A. Jain, G. Hautier, M. Kocher, S. Cholia, D. Gunter, V. L. Chevrier, K. A. Persson and G. Ceder, *Comput. Mater. Sci.*, 2013, **68**, 314–319.

64 W. Sun and G. Ceder, *Surf. Sci.*, 2013, **617**, 53–59.

65 H. Zhuang, A. J. Tkalych and E. A. Carter, *J. Phys. Chem. C*, 2016, **120**, 23698–23706.

66 A. Dal Corso, A. Pasquarello, A. Baldereschi and R. Car, *Phys. Rev. B: Condens. Matter Mater. Phys.*, 1996, **53**, 1180–1185.

67 P. Haas, F. Tran and P. Blaha, *Phys. Rev. B: Condens. Matter Mater. Phys.*, 2009, **79**, 1–10.

68 W. Tyson and W. Miller, *Surf. Sci.*, 1977, **62**, 267–276.

69 M. Mavrikakis, B. Hammer and J. K. Nørskov, *Phys. Rev. Lett.*, 1998, **81**, 2819–2822.

70 P. Statiris, H. C. Lu and T. Gustafsson, *Phys. Rev. Lett.*, 1994, **72**, 3574–3577.

71 R. J. Culbertson, L. C. Feldman, P. J. Silverman and H. Boehm, *Phys. Rev. Lett.*, 1981, **47**, 657–660.

72 N. H. De Leeuw and C. J. Nelson, *J. Phys. Chem. B*, 2003, **107**, 3528–3534.

73 M. Methfessel, D. Hennig and M. Scheffler, *Phys. Rev. B: Condens. Matter Mater. Phys.*, 1992, **46**, 4816–4829.

74 X. Q. F. Jun Wan, Y. L. Fan, D. W. Gong and S. G. Shen, *Model. Simul. Mater. Sci. Eng.*, 1999, **7**, 189–206.

75 Y. Wang, W. Wang, K. N. Fan and J. Deng, *Surf. Sci.*, 2001, **490**, 125–132.

76 K. Letchworth-Weaver and T. A. Arias, *Phys. Rev. B: Condens. Matter Mater. Phys.*, 2012, **86**, 1–16.

77 J. Le, M. Iannuzzi, A. Cuesta and J. Cheng, *Phys. Rev. Lett.*, 2017, **119**, 1–6.

78 A. Frumkin and O. Petrii, *Electrochim. Acta*, 1975, **20**, 347–359.

79 K. Mathew, R. Sundararaman, K. Letchworth-Weaver, T. A. Arias and R. G. Hennig, *J. Chem. Phys.*, 2014, **140**, 084106.

80 J. Y. Lee, M. P. Punkkinen, S. Schönecker, Z. Nabi, K. Kádas, V. Zólyomi, Y. M. Koo, Q. M. Hu, R. Ahuja, B. Johansson, J. Kollár, L. Vitos and S. K. Kwon, *Surf. Sci.*, 2018, **674**, 51–68.

81 Y. Kuk and L. C. Feldman, *Phys. Rev. B: Condens. Matter Mater. Phys.*, 1984, **30**, 5811–5816.

82 R. J. Nichols, T. Nouar, C. A. Lucas, W. Haiss and W. A. Hofer, *Surf. Sci.*, 2002, **513**, 263–271.

83 S. Å. Lindgren, L. Walldén, J. Rundgren and P. Westrin, *Phys. Rev. B: Condens. Matter Mater. Phys.*, 1984, **29**, 576–588.

84 K. Krupski, M. Moors, P. Jóźwik, T. Kobiela and A. Krupski, *Materials*, 2015, **8**, 2935–2952.

85 N. Materer, A. Barbieri, D. Gardin, U. Starke, J. D. Batteas, M. A. Van Hove and G. A. Somorjai, *Surf. Sci.*, 1994, **303**, 319–332.

86 K. P. Huber and G. Herzberg, *Molecular Spectra and Molecular Structure*, Springer US, Boston, MA, 1979.

87 D. M. Cooper, S. R. Langhoff, D. M. Cooper and S. R. Langhoff, *J. Chem. Phys.*, 1981, **74**(2), 1200–1210.

88 L. A. Barnes, B. Liu and R. Lindh, *J. Chem. Phys.*, 1993, **98**, 3972–3976.

89 J. P. Perdew, K. Burke and Y. Wang, *Phys. Rev. B: Condens. Matter Mater. Phys.*, 1996, **54**, 16533–16539.

90 J. P. Perdew, A. Ruzsinszky, G. I. Csonka, O. A. Vydrov, G. E. Scuseria, L. A. Constantin, X. Zhou and K. Burke, *Phys. Rev. Lett.*, 2008, **100**, 136406.

91 J. Tao, J. P. Perdew, V. N. Staroverov and G. E. Scuseria, *Phys. Rev. Lett.*, 2003, **91**, 146401.

92 J. P. Perdew, A. Ruzsinszky, G. I. Csonka, L. A. Constantin and J. Sun, *Phys. Rev. Lett.*, 2009, **103**, 026403.

93 S. Vollmer, G. Witte and C. Wöll, *Catal. Lett.*, 2001, **77**, 97–101.

94 F. Abild-Pedersen and M. P. Andersson, *Surf. Sci.*, 2007, **601**, 1747–1753.

95 A. Patra, H. Peng, J. Sun and J. P. Perdew, *Phys. Rev. B*, 2019, **100**, 1–8.

96 M. Gajdo, A. Eichler and J. Hafner, *J. Phys.: Condens. Matter*, 2004, **16**, 1141–1164.

97 G. Kresse, A. Gil and P. Sautet, *Phys. Rev. B: Condens. Matter Mater. Phys.*, 2003, **68**, 3–6.

98 Y. Wang, S. De Gironcoli, N. S. Hush and J. R. Reimers, *J. Am. Chem. Soc.*, 2007, **129**, 10402–10407.

99 K. G. Lakshmikanth, I. Kundappaden and R. Chatanathodi, *Surf. Sci.*, 2019, **681**, 143–148.

100 L. Köhler and G. Kresse, *Phys. Rev. B: Condens. Matter Mater. Phys.*, 2004, **70**, 1–9.

101 M. Gajdoš and J. Hafner, *Surf. Sci.*, 2005, **590**, 117–126.

102 P. Philipsen, E. van Lenthe, J. Snijders and E. Baerends, *Phys. Rev. B: Condens. Matter Mater. Phys.*, 1997, **56**, 13556–13562.

103 M. Alaei, H. Akbarzadeh, H. Gholizadeh and S. de Gironcoli, *Phys. Rev. B: Condens. Matter Mater. Phys.*, 2008, **77**, 085414.

104 S. Sharifzadeh, P. Huang and E. Carter, *J. Phys. Chem. C*, 2008, **112**, 4649–4657.

105 W.-L. Li, C. N. Lininger, V. V. Welborn, E. Rossomme, A. T. Bell, M. Head-Gordon and T. Head-Gordon, *Statistical Mechanics Improves Density Functional Theory for Electrocatalytic Metal Surface Properties and CO Binding Trends*, 2020.

106 B. Hammer and J. Nørskov, *Adv. Catal.*, 2000, **45**, 71–129.

107 A. Föhlisch, M. Nyberg, P. Bennich, L. Triguero, J. Hasselström, O. Karis, L. G. M. Pettersson and A. Nilsson, *J. Chem. Phys.*, 2000, **112**, 1946–1958.

108 B. Hammer, Y. Morikawa and J. K. Nørskov, *Phys. Rev. Lett.*, 1996, **76**, 2141–2144.

109 N. Mardirossian and M. Head-Gordon, *Phys. Chem. Chem. Phys.*, 2014, **16**, 9904–9924.

110 P. Jurečka, J. Šponer, J. Černý and P. Hobza, *Phys. Chem. Chem. Phys.*, 2006, **8**, 1985–1993.

111 Y. N. Kalugina, A. Faure, A. van der Avoird, K. Walker and F. Lique, *Phys. Chem. Chem. Phys.*, 2018, **20**, 5469–5477.